The Journal of Chemical Physics ARTICLE scitation.org/journal/jcp

Molecular dynamics study of six-dimensional hard hypersphere crystals

Cite as: J. Chem. Phys. 155, 144502 (2021); doi: 10.1063/5.0066421
Submitted: 10 August 2021 • Accepted: 27 September 2021 •
Published Online: 11 October 2021

Leo Lue,[1,a)] Marvin Bishop,[2] and Paula A. Whitlock[3]

AFFILIATIONS

[1] Department of Chemical and Process Engineering, University of Strathclyde, James Weir Building, 75 Montrose Street, Glasgow G11XJ, United Kingdom
[2] Department of Mathematics, Manhattan College, Manhattan College Parkway, Riverdale, New York, New York 10471, USA
[3] Department of Computer and Information Sciences, Brooklyn College, 2900 Bedford Avenue, Brooklyn, New York, New York 11210, USA

[a)] **Author to whom correspondence should be addressed:** leo.lue@strath.ac.uk

ABSTRACT

Six-dimensional hard hypersphere systems in the A_6, D_6, and E_6 crystalline phases have been studied using event-driven molecular dynamics simulations in periodic, skew cells that reflect the underlying lattices. In all the simulations, the systems had sufficient numbers of hyperspheres to capture the first coordination shells, and the larger simulations also included the complete second coordination shell. The equations of state, for densities spanning the fluid, metastable fluid, and solid regimes, were determined. Using molecular dynamics simulations with the hyperspheres tethered to lattice sites allowed the computation of the free energy for each of the crystal lattices relative to the fluid phase. From these free energies, the fluid–crystal coexistence region was determined for the E_6, D_6, and A_6 lattices. Pair correlation functions for all the examined states were computed. Interestingly, for all the states examined, the pair correlation functions displayed neither a split second peak nor a shoulder in the second peak. These behaviors have been previously used as a signature of the freezing of the fluid phase for hard hyperspheres in two to five dimensions.

I. INTRODUCTION

Research into systems in arbitrary spatial dimensions is an active area of inquiry in a variety of fields. Examples of the rich diversity of applications include the study of proton stability in the six-dimensional standard model,[1] quantum field theories,[2] Ising spin glasses,[3] studies of mutually unbiased bases,[4] and wave packet methods for quantum dynamics.[5] Other research areas that focus on six-dimensional systems include quantum key distribution,[6] mapping the movements of autonomous mobile robots,[7] biological applications,[8] percolation in high dimensions,[9,10] and data mining methods with multi-dimensional data.[11,12]

Hard hypersphere systems in arbitrary spatial dimensions have been and remain an active area of research in statistical mechanics.[13–18] The symmetries of the lattices in multidimensional systems have been studied by researchers in discrete geometry and number theory as well as coding theory.[19,20] Six-dimensional hypersphere systems are of particular interest[13–18] because there are three thermodynamically stable crystalline lattices,[19] A_6, D_6, and E_6. The E_6 lattice is the densest of these lattices and has the lowest free energy.[21] Similarly to hard hypersphere systems in lower dimensions, there is a transition from a fluid state at low densities to a crystalline state at higher densities. The variation of the pressure with density can be used to indicate the transition as the density is increased. Compared to systems at a lower dimension, the fluid–crystal transition is observed at higher densities. Frisch and coworkers[13,14,22] demonstrated theoretically that for repulsive potentials, all virial coefficients beyond the second vanish as the dimension approaches infinity. In addition, the work of Torquato *et al.*[23,24] proposed a "decorrelation principle" which states that unconstrained spatial correlations diminish as the dimension increases and vanish in the $d \to \infty$ limit. One result of this behavior is the formation of the crystalline state at higher densities; another reason is that the six-dimensional systems experience greater geometrical frustration.[21]

This paper extends earlier work that reported on six-dimensional Monte Carlo (MC) and molecular dynamics (MD)

calculations in the fluid and high density metastable regimes.[25,26] Here, we present MD simulations of the crystalline phases of six-dimensional hard hyperspheres. In most previous work on higher dimension hard hypersphere systems, the simulations are performed in periodic boxes where the sides of the primary simulation cell are orthogonal. This severely restricts the system sizes (i.e., the number of hyperspheres in the system) for a particular lattice type. In this work, we perform simulations for different six-dimensional hard hypersphere crystals in skew periodic boxes, where the edges are aligned with the basis vectors of the lattice. This allows the analysis of a wider range of distinct system sizes for a given lattice.

The remainder of this paper is organized as follows: In Sec. II, the details of the simulations are presented. Then, in Sec. III, the MD simulation results for the compressibility factor Z are compared with previous MC and MD calculations in both the fluid and solid phases. The MD results for the three different lattices are compared with theoretical equations of state (EOS) based on the extension of Speedy's[27] work in three dimensions by Pieprzyk and co-workers.[28] A recent theoretical prediction of the fluid EOS by Amorós and Ravi[29] is compared with previously reported simulation results. In Sec. IV, we perform MD simulations of tethered systems to calculate the free energy of each of the crystalline phases. These are then used to determine their coexistence point with the fluid phase. In Sec. V, the structure of the hard hypersphere systems is examined, both in the different crystalline lattices and in the fluid phase. Finally, Sec. VI summarizes the main results of this work.

TABLE I. Basis vectors for the A_6, D_6, and E_6 lattices.

	$\mathbf{a}_1$	$\mathbf{a}_2$	$\mathbf{a}_3$	$\mathbf{a}_4$	$\mathbf{a}_5$	$\mathbf{a}_6$
A_6	1	0	0	0	0	0
	−1	1	0	0	0	0
	0	−1	1	0	0	0
	0	0	−1	1	0	0
	0	0	0	−1	1	0
	0	0	0	0	−1	1
	0	0	0	0	0	−1
D_6	1	1	0	0	0	0
	1	−1	1	0	0	0
	0	0	−1	1	0	0
	0	0	0	−1	1	0
	0	0	0	0	−1	1
	0	0	0	0	0	−1
E_6	0	0	0	0	0	1/2
	−1	0	0	0	0	1/2
	1	−1	0	0	0	1/2
	0	1	−1	0	0	1/2
	0	0	1	−1	0	−1/2
	0	0	0	1	−1	−1/2
	0	0	0	0	1	−1/2
	0	0	0	0	0	−1/2

II. SIMULATION DETAILS

We perform event-driven MD simulations over a range of densities for $d = 6$ dimensional hard hyperspheres. The algorithms used in the simulations are generalizations of the standard method originally developed by Alder and Wainwright[30,31] for three-dimensional hard sphere systems. To calculate the free energy of the hard hypersphere systems, we consider a system where each particle is tethered to a lattice site, which forces it to remain a fixed distance r_T (which we refer to as the tether length) from the site. This model was originally introduced by Speedy[32] and has been used to calculate the free energy of hard sphere systems in three dimensions.[32,33] For these systems, an additional event is considered when a particle "collides" with its tether and is reflected back toward its lattice site. In cases where the tether length is short, a stochastic Andersen thermostat[34] is used to increase the equilibration rate.

Unlike previous work, the calculations were performed in skew simulation boxes where the edges were aligned with the basis vectors of the respective lattice of the system, and the corresponding periodic boundary conditions were imposed by evaluating the distances between hyperspheres using the minimum-image convention.

The basis vectors[35] for the A_6, D_6, and E_6 lattices used in this work are summarized in Table I. For the E_6 lattice, three system sizes were examined. The smallest simulation box consisted of $3 \times 5 \times 7 \times 5 \times 3 \times 5$ unit cells. This means that the lattice was constructed by taking a hypersphere and combining it with every combination of up to three translations along the basis vector $\mathbf{a}_1$, five translations along $\mathbf{a}_2$, seven translations along $\mathbf{a}_3$, five translations along $\mathbf{a}_4$, three translations along $\mathbf{a}_5$, and five translations along $\mathbf{a}_6$ for a total of $N = 7875$ hyperspheres. A larger box has $5 \times 5 \times 7 \times 5 \times 5 \times 5$ unit cells and $N = 21\,875$, and the largest box has $5 \times 7 \times 9 \times 7 \times 5 \times 5$ and $N = 55\,125$. For the D_6 lattice, simulations were performed for a box with $5 \times 5 \times 5 \times 5 \times 5 \times 5$ unit cells with a total of $N = 15\,625$ hyperspheres and a larger box with $5 \times 5 \times 7 \times 7 \times 5 \times 5$ unit cells with a total of $N = 30\,625$ hyperspheres. These simulations were compared to Monte Carlo calculations for $N = 23\,328$ hyperspheres initially started in a D_6 lattice in a hypercubic simulation box over a range of densities encompassing both the fluid and solid phases. The results for the pair correlation functions between the MD simulation in the skew boxes and the MC simulations in the hypercubic boxes were in very close agreement. For the A_6 lattice, the simulation box contained $5 \times 5 \times 5 \times 5 \times 5 \times 5$ unit cells with a total of $N = 15\,625$ hyperspheres.

These particular simulation cell sizes were chosen to ensure that the number of hyperspheres in the first coordination shell of each hypersphere is equal to the kissing number[19] of the lattice. If the simulation cell is naively chosen, this will not be the case. For example, a $5 \times 5 \times 5 \times 5 \times 5 \times 5$ simulation box for the E_6 lattice would lead to 68 nearest neighbors for each hypersphere, whereas the kissing number[19] is 72. If all the nearest neighbors are not included in a simulation cell, there is a possibility that collisions between hyperspheres can be missed, leading to hypersphere overlap and premature termination of the simulation.

The MD simulations are performed in batches of 10^6 collisions. The hyperspheres were initialized in the A_6, D_6, and E_6 lattices. For each set of conditions, a series of initial equilibration simulations were run until the pressure of the system fluctuated around a steady state value. Typically, an equilibration period lasted for 10^6 collisions; however, when the system transitioned from a lattice phase to the fluid phase, a longer period was used to equilibrate the simulations. The properties of the system were collected over a period of

10^7 collisions in batches of 10^6 collisions, with the value reported as the mean of these runs and the uncertainty estimated by the standard deviation of the mean.

The contact value of the radial distribution function $G(\sigma)$ can be determined directly from the collision rate through the relationship[36]

$$G(\sigma) = \frac{1}{\rho B_2} \frac{(\pi\beta m\sigma^2)^{1/2} N_{\text{coll}}}{dN\tau}, \tag{1}$$

where τ is the duration of the simulation, $\mathcal{N}_{\text{coll}}$ is the total number of collisions between hyperspheres, $\beta = 1/(k_B T)$, k_B is the Boltzmann constant, T is the absolute temperature of the system, m is the mass, ρ is the number density, and σ is the diameter of a hypersphere. B_2 is the second virial coefficient, which is given by[37]

$$B_2 = \frac{\pi^{d/2}\sigma^d}{2\Gamma(1 + d/2)}, \tag{2}$$

where Γ is the Gamma function.

The equation of state of a system relates its pressure P, temperature T, and ρ. The EOS is typically reported in terms of the compressibility factor $Z = \beta P/\rho$, which quantifies the deviations of the pressure from that of an ideal gas. The compressibility factor can be computed through the virial theorem, which for a hard hypersphere system is related to the collision rate[36]

$$Z = 1 + \frac{\beta m\sigma}{d} \frac{N_{\text{coll}}}{N\tau} \langle \hat{\mathbf{r}}_{ij} \cdot \Delta\mathbf{v}_i \rangle_{\text{coll}}, \tag{3}$$

where $\Delta\mathbf{v}_i$ is the change of the velocity of hypersphere i, $\hat{\mathbf{r}}_{ij}$ is a unit vector that points from the center of hypersphere j to the center of hypersphere i, and the symbol $\langle \cdots \rangle_{\text{coll}}$ indicates that the average is taken on collision.

This equation can be recast as[36]

$$Z = 1 + \frac{(\pi\beta m\sigma^2)^{1/2} N_{\text{coll}}}{dN\tau}. \tag{4}$$

Note that the compressibility factor can also be determined from the contact value of the pair correlation function[38] by

$$Z = 1 + \rho B_2 G(\sigma). \tag{5}$$

III. EQUATION OF STATE

The compressibility factor was calculated from the MD simulations using both Eqs. (4) and (5); the results from both methods agreed within one standard error. Table II reports the MD compressibility factor using Eq. (4) for the A_6, D_6, and E_6 lattices for systems with a different number N of hyperspheres, compared to previous MC results by van Meel *et al.*[21] The excellent agreement at all values of density indicates that the systems studied are sufficiently large to minimize any size dependence. The large Z values found for the A_6 lattice at $\rho\sigma^6 = 3.0$ and the E_6 lattices at $\rho\sigma^6 = 4.6$ are caused by these densities being nearly at the close packed densities, $8/\sqrt{7} \approx 3.0237$ and $8/\sqrt{3} \approx 4.6188$, respectively, as given in Table III.

TABLE II. Compressibility factors for the A_6, D_6, and E_6 lattice systems.

	A_6		D_6		E_6			
$\rho\sigma^d$	15 625	15 625	30 625	Refs. 21 and 39	7875	21 875	55 125	Refs. 21 and 39
1.0	6.73(2)	6.72(3)	6.72(7)	6.71	6.72(2)	6.72(2)	6.72(07)	6.73
1.2	8.98(3)	8.97(1)	8.97(7)	⋯	8.96(3)	8.96(1)	8.96(18)	⋯
1.4	11.77(3)	11.81(4)	11.78(12)	11.81	11.77(3)	11.78(3)	11.77(10)	11.78
1.5	11.84(5)	8.57(3)	8.55(10)	8.59	7.49(3)	7.48(2)	7.48(07)	7.49
1.6	11.81(2)	8.60(2)	8.61(9)	⋯	7.54(1)	7.56(2)	7.55(07)	⋯
1.8	13.53(2)	9.27(1)	9.26(6)	⋯	8.02(1)	8.02(1)	8.02(06)	⋯
2.0	16.27(3)	10.25(1)	10.25(6)	10.25	8.69(1)	8.69(1)	8.68(08)	8.69
2.2	20.49(3)	11.53(1)	11.53(6)	⋯	9.52(1)	9.52(2)	9.52(07)	⋯
2.4	27.50(3)	13.17(1)	13.17(6)	⋯	10.53(1)	10.53(1)	10.53(05)	⋯
2.6	41.19(6)	15.29(2)	15.29(5)	⋯	11.75(1)	11.75(1)	11.75(06)	⋯
2.8	79.46(13)	18.14(2)	18.14(8)	⋯	13.26(1)	13.26(1)	13.26(07)	⋯
3.0	763.28(55)	22.14(3)	22.13(9)	⋯	15.14(1)	15.14(2)	15.14(12)	⋯
3.2	⋯	28.13(2)	28.13(13)	⋯	17.56(1)	17.56(2)	17.56(06)	⋯
3.4	⋯	38.13(3)	38.13(21)	⋯	20.77(1)	20.77(2)	20.77(12)	⋯
3.6	⋯	58.14(4)	58.16(24)	⋯	25.24(2)	25.24(3)	25.24(12)	⋯
3.8	⋯	118.13(13)	118.17(68)	⋯	31.89(1)	31.89(3)	31.89(18)	⋯
3.9	⋯	238.11(21)	238.17(75)	⋯	⋯	⋯	⋯	⋯
4.0	⋯	⋯	⋯	⋯	42.83(3)	42.84(3)	42.84(19)	⋯
4.2	⋯	⋯	⋯	⋯	64.23(3)	64.23(8)	64.24(48)	⋯
4.3	⋯	⋯	⋯	⋯	84.99(6)	85.00(7)	85.01(50)	⋯
4.4	⋯	⋯	⋯	⋯	124.72(8)	124.72(10)	124.76(42)	⋯
4.5	⋯	⋯	⋯	⋯	231.29(14)	231.34(29)	231.25(87)	⋯
4.6	⋯	⋯	⋯	⋯	1471.6(7)	1471.8(11)	1471.41(79)	⋯

TABLE III. Fitted parameters for Eq. (10). The uncertainty of the final digit is given in parentheses.

Lattice	N	A	B	C	ρ_c
A_6	15 625	−1.620(1)	$0.355(1) \times 10^{-2}$	11.19(1)	$8/\sqrt{7}$
D6	15 625	−1.867(1)	$0.133(6) \times 10^{-3}$	13.57(0)	4
D6	30 625	−1.862(2)	$0.711(3) \times 10^{-4}$	14.64(3)	
E6	7 875	−1.972(3)	$0.426(6) \times 10^{-5}$	17.24(0)	
E6	21 875	−1.977(1)	$0.334(8) \times 10^{-5}$	17.71(0)	$8/\sqrt{3}$
E6	55 125	−1.974(7)	$0.309(6) \times 10^{-5}$	17.78(5)	

Figure 1 presents the compressibility factor for the six-dimensional systems in the fluid, metastable fluid, and solid states. The filled circles, filled up-triangles, and filled down-triangles are the compressibility factors from Table II for the E_6, D_6, and A_6 lattices, respectively. The current MD results are compared to data from van Meel *et al.*[21] for the D_6 lattice (open triangles) and E_6 lattice (open circles). The diamonds and squares are previously reported MC[25] and MD[26] results, respectively, for high density fluids. The pentagons are fluid and metastable fluid data from van Meel *et al.*[21,39]

In the fluid regime, at low to intermediate densities, Amorós and Ravi[29] extended the Carnahan and Starling[40] (CS) equation of state for hard spheres to higher dimensions. Using the CS approach, they fit the first five calculated virial coefficients[37,41–44] to determine a polynomial equation of state. Their equations in six dimensions for the virial equation Z_V and the CS compressibility factor Z_{CS} are, respectively,

$$Z_V = 1 + 32\eta + 349.12\eta^2 + 1093.23\eta^3 + 7888.54\eta^4 \tag{6}$$

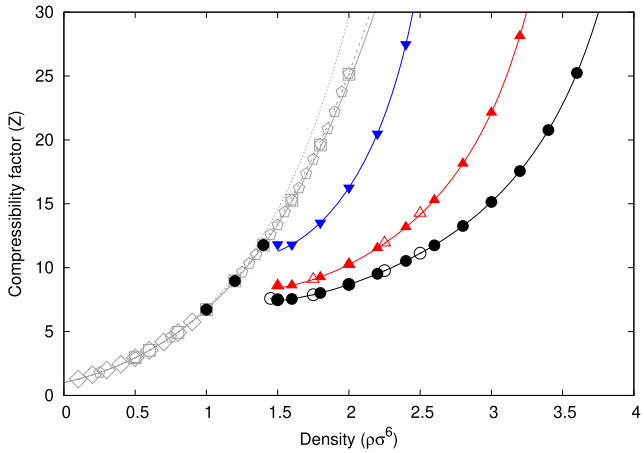

FIG. 1. The compressibility factor for six-dimensional hard hypersphere systems. The filled symbols are the present MD simulation results for the E_6 lattice (circles), D_6 lattice (triangles), and A_6 lattice (down triangles). The open circles and the open up-triangles are the MC data of van Meel *et al.*[21] The solid lines are Eq. (10) with parameters given in Table III. At lower densities, the MC results[25] (diamonds), the MD results[26] (squares), and the MC results[21,39] (pentagons) are displayed. The dotted line is Eq. (7), the dashed line is Eq. (6), and the solid line is Eq. (8).

and

$$Z_{CS} = \frac{1 + 27.76\eta + 227.75\eta^2 - 115.72\eta^3 + 5483.43\eta^4}{(1-\eta)^4}, \tag{7}$$

where $\eta = B_2\rho/2^{d-1}$ is the packing fraction of the hyperspheres. Bishop and Whitlock previously[25] developed a 4, 5-Padé fit of the first ten virial coefficients of the six-dimensional hard hypersphere fluid,[44,45]

$$Z_{[4,5]} = \frac{1 + 5.6358(\rho\sigma^6) + 11.648(\rho\sigma^6)^2 + 10.539(\rho\sigma^6)^3 + 3.417\,0(\rho\sigma^6)^4}{1 + 3.0520(\rho\sigma^6) + 1.485\,7(\rho\sigma^6)^2 - 0.8228(\rho\sigma^6)^3 + 0.0694(\rho\sigma^6)^4 + 0.0154(\rho\sigma^6)^5}. \tag{8}$$

The dotted line in Fig. 1 is the CS equation of state [Eq. (7)], the dashed line is Z_V [Eq. (6)], and the solid curve is Eq. (8). For lower densities, below the E_6 freezing density (estimated[18] to be $\rho\sigma^6 \approx 1.398$), Z_{CS}, Z_V, and $Z_{[4,5]}$ are in excellent agreement with all the simulation data. Above the freezing density, in the metastable liquid regime, Z_{CS} deviates from the simulation data, whereas Z_V as well as $Z_{[4,5]}$ remain in agreement. Amorós and Ravi[29] speculate that this result for Z_{CS} is caused by using only the first five virial coefficients in their fits to the CS equation.

In the MD simulations performed in this work, the compressibility factors at $\rho\sigma^6 = 1.0$, 1.2, and 1.4 are the same across each of the lattices, suggesting that they were all in the fluid phase. In the simulations for $\rho\sigma^6 = 1.0$ and 1.2, all the lattices rapidly melted into the fluid phase; for $\rho\sigma^6 = 1.4$, both the A_6 and D_6 lattices melted quickly, but the E_6 lattice transitioned slowly from the solid phase to the fluid phase.

To describe the equation of state of solids in three dimensions, Speedy[27] developed an empirical equation for hard spheres by fitting his molecular dynamics EOS data,

$$Z_S = \frac{3}{1-\rho/\rho_c} - \frac{C_1(\rho/\rho_c - C_2)}{(\rho/\rho_c - C_3)}, \tag{9}$$

where ρ is the number density, ρ_c is the close packed density, and the constants C_1, C_2, and C_3 are adjusted to reproduce simulation data.

Recently, a detailed investigation[28] of the properties of three-dimensional hard sphere systems using MD with up to about 10^6 particles re-examined the functional form of the EOS in the solid state. Pieprzyk *et al.*[28] proposed several improvements. They fit Speedy's form to their highly accurate simulation data but decided that an exponential form better described the non-free volume portion of the EOS. Following this suggestion, we have tried a

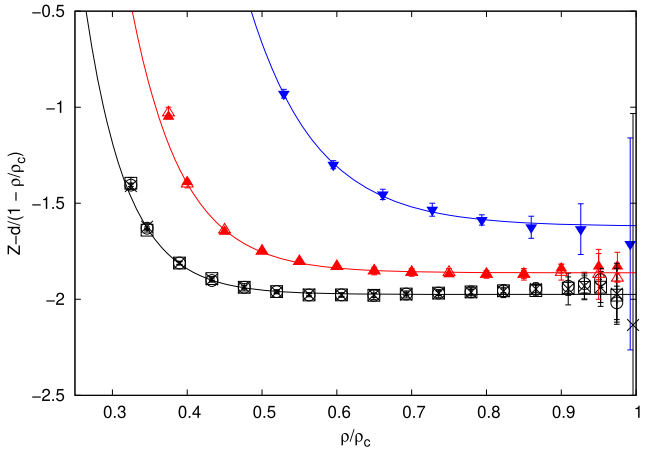

FIG. 2. The solid EOS scaled by the free volume vs the scaled density. The open circles represent the E_6 lattice with $N = 55\,125$, the crosses are $N = 21\,875$, and the open squares are $N = 7875$. The solid red up-triangles are the D_6 data for $N = 30\,625$ and open red triangles are $N = 15\,625$. The blue down triangles are the A_6 data. The solid lines are Eq. (10) scaled by the free volume.

generalized version of their exponential form,[28]

$$Z_{\mathrm{SE}} = \frac{d}{1-\rho/\rho_c} + A + Be^{C(1-\rho/\rho_c)}, \tag{10}$$

which fits the six-dimensional simulation data very well for all solid densities in the three lattice systems. In Fig. 1, the parameters in Eq. (10), shown by the solid lines, were determined by fitting the data for $\rho\sigma^6 \geq 1.6$ in Table II; the fitted parameters for each lattice, as well as the close packed density[19] ρ_c, are summarized in Table III.

To better understand the behavior over the complete range of the crystal data, Fig. 2 plots the non-free volume portion of the compressibility factor Z [i.e., $Z - d/(1-\rho/\rho_c)$] against ρ/ρ_c. The black circles are the E_6 data for $N = 55\,125$ with error bars of one standard deviation, the crosses are for $N = 21\,875$, and the open squares are for $N = 7875$. The filled red triangles are the D_6 data for $N = 30\,625$, and the open red triangles are for $N = 15\,625$. The blue down-triangles are the A_6 data. The solid lines represent Eq. (10). Plotting the data in this manner emphasizes that as the density increases, the free volume behavior dominates and that the constant term in Eq. (10) gives rise to the observed plateau.

IV. ESTIMATION OF FLUID–SOLID COEXISTENCE

At the fluid–solid coexistence point for the hard hypersphere system, the pressures and the chemical potentials of each of the phases are equal. The pressure of a hypersphere system can be directly determined from the MD simulations, whereas the chemical potential cannot. However, the variation of the residual chemical potential with density can be determined directly from knowledge of the compressibility factor. The relation can be written as[33]

$$\beta\mu(\rho) - \beta\mu^{\mathrm{ig}}(\rho_{\mathrm{ref}}) = \ln\frac{\rho}{\rho_{\mathrm{ref}}} + \frac{F^{\mathrm{res}}(\rho_0)}{Nk_BT} + \int_{\rho_0}^{\rho}\frac{d\rho'}{\rho'}[Z(\rho')-1] + Z(\rho) - 1, \tag{11}$$

where ρ_0 is a "starting" density, ρ_{ref} is a reference density, μ^{ig} is the ideal gas chemical potential, and F^{res} is the residual Helmholtz energy (i.e., the Helmholtz energy of the system relative to the Helmholtz energy of an ideal gas system at the same density). For hard hypersphere systems, the only energetic contribution to the free energy is the kinetic energy. Consequently, the residual Helmholtz energy is directly related to the residual entropy S^{res} as $F^{\mathrm{res}} = -TS^{\mathrm{res}}$, which can be determined by considering tethered hard hypersphere systems. Therefore, in the following discussion, we refer to the entropy of the system, rather than the Helmholtz energy.

For a fluid system, the starting density can be conveniently chosen to be $\rho_0 = 0$, where the system behaves ideally, and $S^{\mathrm{res}} = 0$. In the case of a solid system, however, the presence of a first order phase transition does not allow the smooth connection of the state to the ideal gas state, and the starting density $\rho_0 = 0$ cannot be used. Consequently, the residual entropy $S^{\mathrm{res}}(\rho_0)$ needs to be evaluated at some density ρ_0 where the system is in the same solid phase.

In a tethered system, each particle is restricted to remain within a distance r_T, known as the tether length, from a specified lattice site. For a lattice at density ρ, the spacing between sites is $a = (\rho_c/\rho)^{1/d}$, where ρ_c is the maximum density of the lattice (see Table III). If the tether length is less than $r_{T,0} = (a-\sigma)/2$, then the particles are too far apart to interact with each other. The minimum tether length $r_{T,0}$ depends on the density of the system—the higher the density, the shorter the minimum tether length.

When $r_T < r_{T,0}$, the system behaves as an ideal tethered system, where there are no particle–particle interactions. The volume of phase space accessible to the ideal tethered hypersphere system is simply the product of the volumes that each of the tethered particles can individually explore,

$$\Omega^{\mathrm{ideal}}(\rho, r_T) = \left(\frac{\pi^{d/2} r_T^d}{\Gamma(d/2+1)}\right)^N, \tag{12}$$

which should be compared to the entropy of a classical ideal gas,

$$\Omega^{\mathrm{ig}} = \frac{V^N}{N!}. \tag{13}$$

The difference between the entropy of an ideal tether system S^{ideal} and an ideal gas S^{ig} at the same density ρ is

$$S^{\mathrm{ideal}}(\rho) - S^{\mathrm{ig}}(\rho) = N\ln\phi_T + N\ln\frac{N!^{1/N}}{N}, \tag{14}$$

where $\phi_T = \pi^{d/2}\rho\, r_T^d/\Gamma(d/2+1)$ is the volume fraction of space occupied by the tether cells.

In a hard hypersphere system, excluded volume interactions restrict the phase space that can be explored. The tethers further restrict the phase space that the system can access. The rate at which the particles collide with their tethers is proportional to the surface area of the boundary due to the presence of the tethers.[33] As the tethers lengthen, the system can access a larger volume of phase space. By tracking the variation of the surface area with the tether length, through monitoring the tether collision rate, the additional volume of phase space accessible to the system can be determined. In the limit that the tether length becomes infinite, the properties of the tethered system approach those of the original, untethered hard

hypersphere system. Based on this, the entropy of an untethered system can be determined[33] by integrating the tether collision rate $\dot{\mathcal{N}}_T$ with respect to the tether length r_T,

$$\frac{S(\rho)}{Nk_B} - \frac{S^{\text{ideal}}(\rho)}{Nk_B} = \frac{(2\pi\beta m\sigma^2)^{1/2}}{N}\int_{r_{T,0}}^{\infty} dr_T\, \dot{\mathcal{N}}_T(\rho, r_T). \tag{15}$$

The residual entropy S^{res} can be obtained by just accounting for the difference between an ideal tethered system and an ideal gas,

$$\frac{S^{\text{res}}(\rho)}{Nk_B} = \frac{(2\pi\beta m\sigma^2)^{1/2}}{N}\int_{r_{T,0}}^{\infty} dr_T\, \dot{\mathcal{N}}_T(\rho, r_T) + \ln\phi_{T,0} + \ln\frac{N!^{1/N}}{N}, \tag{16}$$

where $\phi_{T,0}$ is the volume fraction of space occupied by the tether cells at the minimum tether length $r_{T,0}$.

Simulations of tethered systems are performed at a reference density $\rho_{\text{ref}}\sigma^6 = \rho_0\sigma^6 = 2$ for systems with different tether lengths r_T. The tether collision rates determined by the MD simulations are shown in Fig. 3 for the A_6 (blue), D_6 (red), and E_6 (black) lattices. The different symbols represent simulation data for different sized systems. The size dependence is not significant for the range of conditions examined. The tether collision rate data for the smallest system of each lattice were fit with a cubic spline, shown by the solid lines in Fig. 3.

The vertical dashed lines denote the minimum tether length $r_{T,0}$ for each lattice at the density $\rho_0\sigma^6 = 2$; $r_{T,0}/\sigma \approx 0.035\,659$, 0.061 231, and 0.074 848 for the A_6, D_6, and E_6 lattices, respectively. At $r_{T,0}$, the tether collision rate equals that of an ideal tethered system, which is $\dot{\mathcal{N}}_T^{\text{ideal}} = N(2\pi\beta m\sigma^2)^{-1/2}d/r_T$ (see the dotted line in Fig. 3). As r_T increases, the tether collision rate rapidly decays to zero. The tether collision rate of the A_6 lattice remains lower than that for the D_6 lattice, which, in turn, is lower than for the E_6 lattice for all tether lengths. The area underneath the collision rate curve is directly related to the entropy of the untethered hard hypersphere system compared to the ideal tethered system. As we can see, this area is larger for the more thermodynamically stable lattice (i.e., $E_6 > D_6 > A_6$) and implies that the entropy is higher, as expected. The residual entropies calculated for each lattice, obtained from the cubic spline fits, are summarized in Table IV.

Once we have determined the entropy of a solid phase with respect to the ideal gas state, we can then determine the variation of the chemical potential of the solid phase with density from knowledge of the dependence of the compressibility factor with density and Eq. (11). The compressibility factors for the A_6, D_6, and E_6 lattices were evaluated using Eq. (10) with the respective values of the coefficients as given in Table III. For the fluid phase, the compressibility factor is evaluated using the 4, 5-Padé approximant,[25] shown in Eq. (8).

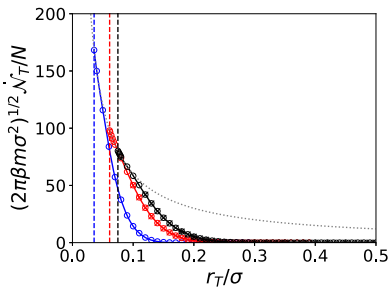

FIG. 3. The tether collision rate as a function of the tether length r_T for the A_6 (blue), D_6 (red; circles: N = 15 625, crosses: N = 30 625), and E_6 (black; circles: N = 7875, crosses: N = 21 875, pluses: N = 55 125) lattices. The black dotted line is the tether collision rate for an ideal tethered system. The vertical dashed lines denote the critical tether length for each respective lattice.

TABLE IV. Data from tether simulations for fluid–solid coexistence calculations for d = 6 dimensional hard hypersphere systems. The reference density $\rho_{\text{ref}}\sigma^d = 2$.

	A_6	D_6	E_6
$S^{\text{res}}(\rho_{\text{ref}})/(Nk_B)$	−13.767(3)	−10.856(3)	−9.815(3)
$\rho_f\sigma^d$	2.1959(7)	1.5531(4)	1.3990(4)
$\rho_s\sigma^d$	2.4063(5)	2.0784(8)	1.9399(10)
$\beta p\sigma^d$	66.90(7)	22.26(2)	16.42(1)
$\beta\mu(\rho_{f/s}) - \beta\mu^{\text{ig}}(\rho_{\text{ref}})$	44.43(3)	20.97(1)	17.02(1)

The variation of the pressure with chemical potential is shown in Fig. 4 for the fluid A_6, D_6, and E_6 phases of the hard hypersphere system. Each line is calculated parametrically with respect to the system density for the respective phase. The slope of the tangent to the curves corresponds to the density of the system. The slope increases with the pressure of the system and is greater for the solid phases than for the fluid phase. The point at which the two curves intersect corresponds to the coexistence between two phases, directly yielding the coexistence pressure and chemical potential. The value of the densities in the respective phases at which this occurs corresponds to the freezing and melting densities. Estimates of the fluid–solid coexistence point for the fluid and each of the lattice phases are summarized in Table IV.

Several authors have previously estimated the location of the fluid–solid coexistence point for the E_6 lattice. Using scaled particle theory to describe the fluid phase and cell theory to model the solid phase, Finken *et al.* estimated[15] the coexisting fluid and solid packing fractions to be $\eta_f = 0.10$ and $\eta_s = 0.16$, respectively. Using Monte Carlo simulations, van Meel and co-workers estimated[21] the coexistence pressure to be $\beta p\sigma^d = 13.3$ and the coexisting packing fractions as $\eta_f = 0.105$ and $\eta_s = 0.138$. Recently, Charbonneau and co-workers presented calculations[18] for the fluid–solid coexistence point for d = 3 to 10 dimensional hard hypersphere systems using

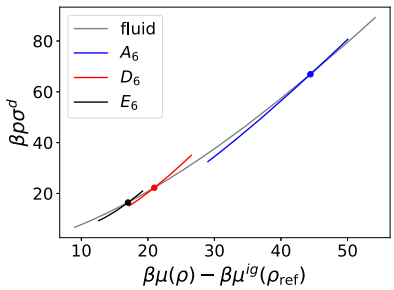

FIG. 4. Variation of the chemical potential with pressure for the fluid phase (gray line), A_6 lattice (blue line), D_6 lattice (red line), and E_6 (black line) lattice. The intersections between curves denote coexistence between phases.

a generalized Frenkel–Ladd method to compute the absolute free energy of the crystalline phases. For the E_6 lattice, they determined the coexistence pressure to be $\beta p\sigma^d = 16.400$, with a fluid packing fraction $\eta_f = 0.1129$ and a solid packing fraction $\eta_s = 0.1567$. In terms of packing fraction, our estimate for the fluid–solid coexistence point for the E_6 lattice occurs at $\eta_f = 0.113$ and $\eta_s = 0.157$, which is in excellent agreement with the values of Charbonneau and co-workers.

The coexistence points for the A_6 and D_6 lattices are shown in Table IV. As the thermodynamic stability of the lattice decreases, the coexistence pressure, as well as the freezing and melting densities, increases.

V. STRUCTURE

Figure 5 displays the pair correlation functions (PCFs) in six dimensions including the liquid phase, at $\rho\sigma^6 = 1.0$, to a fully formed solid phase, at $\rho\sigma^6 = 2.4$, for all three lattice types. Note that for all

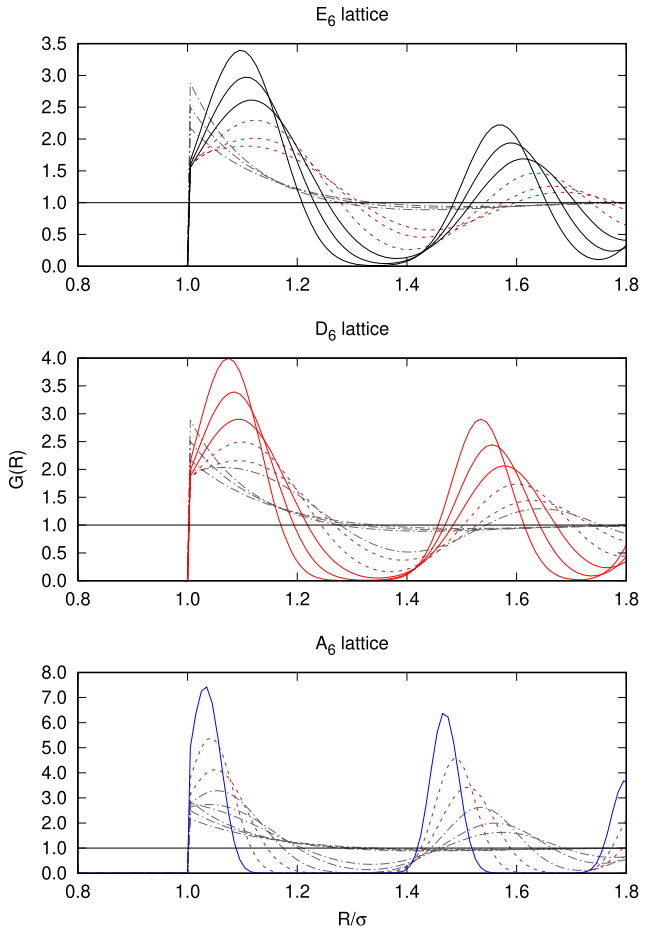

FIG. 5. The pair correlation functions for the E_6, D_6, and A_6 lattice systems at densities $\rho = 1.0$, 1.2, 1.4, 1.5, 1.6, 1.8, 2.0, 2.2, and 2.4. The gray dashed-dotted lines are for systems at fluid densities. The brown dashed lines indicate metastable densities. The black, red, and blue lines are in the solid phase.

the $G(R)$'s, the uncertainties are between 10^{-2} and 10^{-3}. Fluid densities are displayed as dashed–dotted gray curves, and states between the freezing and melting densities, as specified by Table IV, are shown in brown dashed lines. The E_6 solid densities are in black, the D_6 lattice in red, and the A_6 lattice in blue. In the fluid phase, the PCFs have a peak at the hypersphere–hypersphere contact distance, which becomes higher as the density increases. In the solid phase, the peaks of the PCFs occur at the spacings of the lattice. As the density increases, the peaks become higher and sharper, approaching a delta function as the density nears the close packing value of the lattice.

It is known that hard hypersphere systems, with only purely repulsive interactions, undergo a phase transition from the fluid to solid state in dimensions two[46,47] through five,[38,48,49] and this is hypothesized to occur at higher dimensions as well.[15,50,51] Figure 1 demonstrates that two distinct phases exist as the compressibility factor varies with density. In lower dimensions, one indicator of the onset of the phase transition is the behavior of the pair correlation function; that is, a shoulder or a split appears on the second peak.[16] Skoge *et al.*[16] commented in their discussion of maximally packed states that the split peak decreases in prominence as the dimension increases from three to six. Similar behavior was noted in the studies of hard hypersphere systems in the fluid and metastable states.[52] In these previous fluid MC and MD work, simulations were initiated from either a D lattice or a Z lattice. Of note in Fig. 5 is the absence of any shoulder or split in the second peak as the fluid phase approaches the freezing density ρ_f for any of the lattices. In the MD simulations in this work, at all densities, the calculations were initiated from the relevant lattice positions. As other authors have discussed,[13,14,22–24] spatial correlations diminish as the dimension increases and the shape (or structure) of the pair correlation function becomes simpler.

It is interesting to note that in lower dimensions, where a shoulder is clearly observed, the close packed lattices are all "D" lattices. Dimension six is the first dimension in which an E lattice appears, and in this dimension, the E_6 lattice is the closest packed lattice and the most thermodynamically stable crystal structure. In hard hypersphere fluids, the geometry of the close packing plays a prominent role in dictating the structure. The change from an underlying D-type lattice to an underlying E-type may help to explain the absence of a split second peak.

Another approach[23,53,54] to examine the structure in the simulation data is to calculate the occupancy number $\mathcal{N}(R)$ by integrating $G(R)$ as a function of R. $\mathcal{N}(R)$ is the total number of particles located within a distance R from a reference particle at the origin,

$$\mathcal{N}(R) = \rho\sigma^d \int_0^R S_d r^{d-1}\, G(r)\, dr \tag{17}$$

where $S_d = 2\pi^{d/2}/\Gamma(d/2)$ is the surface area of a hypersphere.

$\mathcal{N}(R)$ can be compared to the theoretical theta series.[19] The theta series for a lattice encodes the distribution of vector norms in the lattice. It is used to determine properties such as the packing radius, the kissing number, and the packing density. The predicted total number of particles found between a reference particle and the end of a given shell is obtaining by adding up the theta series coefficient for each shell.

The first several terms of the theta series for the A_6, D_6, and E_6 lattices have been computed by enumeration of the lattice vectors

TABLE V. The theta series for various six-dimensional lattices.

	A_6	D_6	E_6
0	1	1	1
1	42	60	72
2	210	252	270
3	350	544	720
4	882	1020	936
5	1050	1560	2160

surrounding a central site. This was done by taking linear combinations of integer multiples of each of the basis vectors $\mathbf{a}_k$ in the lattice (given in Table I),

$$\mathbf{v} = \sum_k m_k \mathbf{a}_k, \tag{18}$$

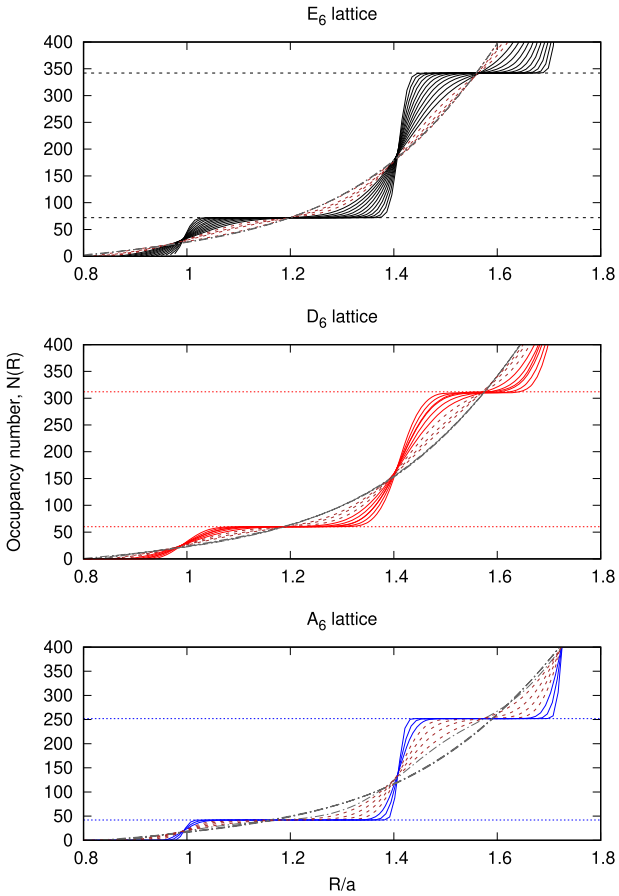

FIG. 6. The occupation numbers for the lattice systems at a series of densities. For the E_6 lattice, the density range is ρ = 1.0–4.0. For the D_6 lattice, the densities range from ρ = 1.0–2.8. The density range is from ρ = 1.0–2.8 for the A_6 lattice. The specific values for the density can be found in Table II. The dashed-dotted gray lines are for systems at fluid densities. The dashed brown lines indicate metastable densities. The solid lines are $\mathcal{N}(R)$ for the crystal densities. The horizontal lines correspond to the shell occupancy values derived from the terms of the theta series for the first two shells of each lattice.

where the integers $m_k \in [-n_{\max}, n_{\max}]$ for some positive integer $n_{\max}$. The lattice sites are ordered in terms of their distance from the central site, and the number of sites in each coordination shell is noted. This process is repeated for successively larger positive integers $n_{\max}$ (up to a value of $n_{\max}$ = 15) to ensure that all the sites within a particular coordination shell have been captured. The first six terms are summarized in Table V and are in complete agreement to those listed in Ref. 55 section A004007 for E_6 and section A008428 for D_6.

The calculated $\mathcal{N}(R)$ for the E_6, D_6, and A_6 lattices is shown in Fig. 6. A range of densities is presented with $\mathcal{N}(R)$ plotted vs R/a, where $a = (\rho_c/\rho)^{1/6}$. The liquid densities are represented by gray dashed-dotted curves, and the metastable densities are represented by brown dashed lines. The horizontal dashed lines in Fig. 6 correspond to the summed terms of the theta series for the respective lattices.

For the E_6 lattice, good agreement is observed for both the first shell value, 72, and the second shell value, 270, even though at ρ = 2.4, the E_6 system is still a somewhat unorganized crystal. The red dotted lines are the sum of the first two terms of the D_6 theta series and agree well with the $\mathcal{N}(R)$ data. At $\rho\sigma^6$ = 2.8, the A_6 system is a well-organized solid, and this is reflected in the behavior of $\mathcal{N}(R)$, which agrees very well with the summed theta series data, the blue dotted line. For all three lattices, the liquid densities, ρ = 1.0, 1.2, and 1.4, fall on the same $\mathcal{N}(R)$ curve.

VI. CONCLUSIONS

In this work, we have used event-driven molecular dynamics to study the crystalline phases of six-dimensional hard hypersphere systems. Unlike most previous work, the simulations were performed in skew boxes, with the edges aligned with basis vectors of the lattice under examination; this allows for a much wider range of system sizes to be explored compared to restricting the box to be hypercubic or hyper-rectangular.

The pressures and thus the compressibility factors in these systems were determined from the particle–particle collision rates, and these were found to be in good agreement with those from previous work. These were found to fit well with the form [Eq. (10)] suggested by Pieprzyk *et al.*[28]

To determine the free energy of the each of the crystalline states, simulations were performed in which the hyperspheres in the system were tethered to a site of the crystalline lattice using an infinite square well of differing widths. As expected, the E_6 structure was found to be more stable than the D_6 structure, which is, in turn, more stable than the A_6 lattice. The fluid–solid coexistence densities and pressure increase in going from the E_6 to the D_6 to the A_6 lattices. The values for the E_6 phase are in excellent agreement with recent Monte Carlo calculations.[18]

The structure of the crystalline phases has been explored through the pair correlation functions. In the solid phase, the pair correlation functions have peaks at distances around the spacing of the lattice sites. As the density of the solid increases, the peaks increase in height and become narrow.

In the fluid phase, the pair correlation functions have peaks at a distance consistent with the hypersphere diameter. For fluid systems near the freezing density, we find no presence of a split second peak or shoulder for fluids near the melting transition. This is in

contrast to what is observed in hard hypersphere systems in two to five dimensions.

Integration of the pair correlation functions to obtain $\mathcal{N}(R)$ shows that the simulations are large enough to encompass the first and second coordination shells of the each of the crystalline phases as well as the fluid phase.

Our studies of multidimensional hypersphere systems are ongoing.

ACKNOWLEDGMENTS

We thank Patrick Charbonneau for sharing data and for useful insights.

AUTHOR DECLARATIONS

Conflict of Interest

The authors have no conflicts to disclose.

DATA AVAILABILITY

The data that support the findings of this study are available from the corresponding author upon reasonable request.

REFERENCES

[1]T. Appelquist, B. A. Dobrescu, E. Pontón, and H.-U. Yee, Phys. Rev. Lett. **87**, 181802 (2001).
[2]V. Kumar and W. Taylor, Adv. Theor. Math. Phys. **15**, 325 (2011).
[3]M. A. Moore and A. J. Bray, Phys. Rev. B **83**, 224408 (2011).
[4]P. Raynal, X. Lü, and B.-G. Englert, Phys. Rev. A **83**, 062303 (2011).
[5]M. T. Cvitaš and S. C. Althorpe, J. Chem. Phys. **134**, 024309 (2011).
[6]N. J. Cerf, M. Bourennane, A. Karlsson, and N. Gisin, Phys. Rev. Lett. **88**, 127902 (2002).
[7]H. Surmann, A. Nüchter, K. Lingemann, and J. Hertzberg, IFAC Proc. Vol. **37**, 197 (2004).
[8]U. H. von Andrian, Science **296**, 1815 (2002).
[9]M. Cheon, M. Heo, I. Chang, and D. Stauffer, Phys. Rev. E **59**, R4733 (1999).
[10]P. Grassberger, Phys. Rev. E **67**, 036101 (2003).
[11]H. R. Khosravani, A. E. Ruano, and P. M. Ferreira, in *2013 IEEE 8th International Symposium on Intelligent Signal Processing* (IEEE, 2013), pp. 109–114.
[12]T. N. Tran, R. Wehrens, and L. M. C. Buydens, Comput. Stat. Data Anal. **51**, 513 (2006).
[13]H. L. Frisch and J. K. Percus, Phys. Rev. A **35**, 4696 (1987).
[14]H. L. Frisch and J. K. Percus, Phys. Rev. E **60**, 2942 (1999).
[15]R. Finken, M. Schmidt, and H. Löwen, Phys. Rev. E **65**, 016108 (2001).
[16]M. Skoge, A. Donev, F. H. Stillinger, and S. Torquato, Phys. Rev. E **74**, 041127 (2006).
[17]S. Torquato, J. Chem. Phys. **149**, 020901 (2018).
[18]P. Charbonneau, C. M. Gish, R. S. Hoy, and P. K. Morse, Eur. Phys. J. E: Soft Matter **44**, 101 (2021).
[19]J. H. Conway and N. J. A. Sloane, *Sphere Packings, Lattices and Groups*, 3rd ed. (Springer-Verlag, New York, 1999).
[20]H. Cohn and N. Elkies, Ann. Math. **157**, 689 (2003).
[21]J. A. van Meel, B. Charbonneau, A. Fortini, and P. Charbonneau, Phys. Rev. E **80**, 061110 (2009).
[22]H. L. Frisch, N. Rivier, and D. Wyler, Phys. Rev. Lett. **54**, 2061 (1985).
[23]S. Torquato, O. U. Uche, and F. H. Stillinger, Phys. Rev. E **74**, 061308 (2006).
[24]G. Zhang and S. Torquato, Phys. Rev. E **88**, 053312 (2013).
[25]M. Bishop and P. A. Whitlock, J. Stat. Phys. **126**, 299 (2007).
[26]L. Lue and M. Bishop, Phys. Rev. E **74**, 021201 (2006).
[27]R. J. Speedy, J. Phys.: Condens. Matter **10**, 4387 (1998).
[28]S. Pieprzyk, M. N. Bannerman, A. C. Brańka, M. Chudak, and D. M. Heyes, Phys. Chem. Chem. Phys. **21**, 6886 (2019).
[29]J. Amorós and S. Ravi, Phys. Lett. A **377**, 2089 (2013).
[30]B. J. Alder and T. E. Wainwright, J. Chem. Phys. **31**, 459 (1959).
[31]M. N. Bannerman, R. Sargant, and L. Lue, J. Comput. Chem. **32**, 3329 (2011).
[32]R. J. Speedy, Mol. Phys. **80**, 1105 (1993).
[33]C. Moir, L. Lue, and M. N. Bannerman, J. Chem. Phys. **155**, 064504 (2021).
[34]H. C. Andersen, J. Chem. Phys. **72**, 2384 (1980).
[35]G. Nebe and N. J. A. Sloane, Lattices: A catalogue of lattices, http://www.math.rwth-aachen.de/ Gabriele.Nebe/LATTICES/, 2019.
[36]L. Lue, J. Chem. Phys. **122**, 044513 (2005).
[37]M. Luban and A. Baram, J. Chem. Phys. **76**, 3233 (1982).
[38]M. Bishop and P. A. Whitlock, J. Chem. Phys. **123**, 014507 (2005).
[39]P. Charbonneau, private communication (2019).
[40]N. F. Carnahan and K. E. Starling, J. Chem. Phys. **51**, 635 (1969).
[41]N. Clisby and B. M. McCoy, J. Stat. Phys. **114**, 1343 (2004).
[42]N. Clisby and B. M. McCoy, J. Stat. Phys. **114**, 1361 (2004).
[43]N. Clisby and B. M. McCoy, Pramana **64**, 775 (2005).
[44]N. Clisby and B. M. McCoy, J. Stat. Phys. **122**, 15 (2006).
[45]N. Clisby, Ph.D. thesis, SUNY, Department of Physics, Stoney Brook, 2004.
[46]B. J. Alder and T. E. Wainwright, Phys. Rev. **127**, 359 (1962).
[47]W. W. Wood, in *Physics of Simple Liquids*, edited by H. N. V. Temperley, J. S. Rowlinson, and G. S. Rushbrooke (North-Holland, Amsterdam, 1968), Chap. V.
[48]B. J. Alder and T. E. Wainwright, J. Chem. Phys. **27**, 1208 (1957).
[49]J. P. J. Michels and N. J. Trappeniers, Phys. Lett. A **104**, 425 (1984).
[50]J.-L. Colot and M. Baus, Phys. Lett. A **119**, 135 (1986).
[51]B. Bagchi and S. A. Rice, J. Chem. Phys. **88**, 1177 (1988).
[52]P. A. Whitlock, M. Bishop, and J. L. Tiglias, J. Chem. Phys. **126**, 224505 (2007).
[53]A. Donev, S. Torquato, and F. H. Stillinger, Phys. Rev. E **71**, 011105 (2005).
[54]L. Lue, M. Bishop, and P. A. Whitlock, J. Chem. Phys. **132**, 104509 (2010).
[55]N. J. A. Sloane, The on-line encyclopedia of integer sequences, http://oeis.org/, 2019.